




Simultaneous analysis of elastic scattering and fusion in ${}^6\text{He} + {}^{64}\text{Zn}$: A transition in direct reaction mechanisms, striking threshold anomalies, and halo effects

E. F. Aguilera ^{1,*}, F. Torabi ¹ and J. C. Morales-Rivera ^{1,2}

¹*Departamento de Aceleradores y Estudio de Materiales, Instituto Nacional de Investigaciones Nucleares, Apartado Postal 18-1027, Código Postal 11801, México, Distrito Federal, México*

²*Facultad de Ciencias, Universidad Autónoma del Estado de México, Instituto Literario 100, Código Postal 50000, Toluca, México*



(Received 2 September 2021; revised 11 October 2021; accepted 15 November 2021; published 29 November 2021)

Using the extended optical model, a simultaneous analysis is carried out of elastic scattering and fusion reactions induced by the neutron halo ${}^6\text{He}$ projectile on a ${}^{64}\text{Zn}$ target. Dynamic polarization potentials U_F, U_D are introduced which can be associated to fusion and direct couplings, respectively. Appropriate fitting parameters leading to dispersive potentials are found which provide a good simultaneous description of the data. An unexpected local maximum is uncovered in the energy dependence of the total reaction cross sections, indicating a transition in the involved direct reaction processes, and a possible underlying mechanism is discussed. U_F is found to follow the normal threshold anomaly but with an unusually large threshold energy. U_D , on the other hand, exhibits a breakup threshold anomaly, but with a strikingly high value of the peak energy, which can be associated to the above-mentioned transition. The results also are discussed within the context of possible halo effects.

DOI: [10.1103/PhysRevC.104.054612](https://doi.org/10.1103/PhysRevC.104.054612)

I. INTRODUCTION

Many studies involving nuclear reactions induced by weakly bound heavy ions, stable or radioactive, have appeared in literature in the latter few decades [1–4]. Among the radioactive nuclear projectiles, those having a halo have been at the forefront of current research worldwide because of their unique, unexpected features. Haloes are a consequence of the weak binding of the last one or two valence nucleons, whose corresponding wave function leads to an extended cloud of diffuse nuclear matter surrounding a relatively stable core. It has been found that for halo nuclei there is a general dominance of direct reactions over fusion at near and sub-barrier energies with important contributions of neutron transfer processes [1]. Within this context, perhaps the most studied light halo nucleus is ${}^6\text{He}$ [2,4], partially due to the relative ease of producing fairly intense beams of it at energies around the Coulomb barrier [4]. In addition to having a two-neutron halo [5], ${}^6\text{He}$ is also an interesting object of study because of its Borromean feature [6], whereby separation of any one of three clusters in (${}^4\text{He} + n + n$) leads to an unbound system.

Several reaction mechanisms such as fusion, transfer, and breakup have been studied with interesting and sometimes astonishing results, as reviewed for instance in Refs. [1,3,4]. Measurements of the elastic scattering process, which is usually considered a rather simple phenomenon, have also provided interesting new perspectives [2].

Considering only medium-mass targets, the ${}^6\text{He} + {}^{64}\text{Zn}$ measurements reported in [7–10] constitute perhaps the most

complete set of ${}^6\text{He}$ data around the Coulomb barrier. Previous analyses of this system have focused either on the elastic scattering or the fusion data separately, but no simultaneous description of both processes has been given so far. In Ref. [8], for instance, the optical model potential extracted from the elastic scattering data was used in a fusion calculation with the CCFULL code [11], but the fusion data were considerably overestimated. A different potential, having a considerably reduced radius, was necessary to describe the fusion excitation function. On the other hand, Crema *et al.* [12] used the São Paulo potential (SPP) [13] to calculate the fusion cross sections for ${}^6\text{He}$ projectiles on several targets, including ${}^{64}\text{Zn}$. By introducing appropriate coupled channels within a barrier penetration model (BPM), the corresponding fusion data for all analyzed systems could be coherently interpreted with the conclusion that the SPP provides an appropriate bare potential to describe fusion (see also Ref. [14]). However, it can be shown that the SPP by itself cannot reproduce the elastic scattering data, even if an interior imaginary potential is introduced to simulate the BPM calculations for fusion [see Eq. (1)]. It was actually suggested in Ref. [14] that, unless full coupled channel calculations are performed (which is presently out of reach), it becomes necessary to add appropriate polarization potentials to the SPP, with possibly very significant contributions. Some authors have in fact questioned the use of the same optical potential to explain simultaneously fusion and quasielastic experimental data [15]. The aim of the present work is to obtain an optical potential that can simultaneously describe data for two processes: the elastic scattering angular distributions reported in [8,10], and the fusion excitation function obtained in [8,9] for the ${}^6\text{He} + {}^{64}\text{Zn}$ system.

*eli.aguilera@inin.gob.mx

A common framework will be used in the analysis of the two processes, following a similar procedure to that used in a recent work [16], where a systematic study of elastic scattering and fusion of the stable, weakly bound nucleus ${}^6\text{Li}$ with the four targets ${}^{58}\text{Ni}$, ${}^{59}\text{Co}$, ${}^{64}\text{Ni}$, and ${}^{64}\text{Zn}$ was performed. The so-called extended optical model (EOM) introduced by Udagawa and Tamura in the 1980s [17,18] was used in that study. In this model, two types of polarization potentials are introduced in the optical potential, which can be associated to direct and fusion couplings, respectively. One interesting feature of this model is that phenomenological potentials can be found which provide simultaneous descriptions for both the elastic scattering and the fusion data in the overlapping energy region where both processes have been measured. The obtained potentials do satisfy the dispersion relation [19,20] and it was actually shown in Ref. [16] that the constraint of having dispersive potentials might be useful to identify seemingly unphysical data; in addition, it can help eliminate possible ambiguities in the parameters of the EOM potential.

It was also concluded in Ref. [16] that, for all ${}^6\text{Li}$ -projectile systems mentioned above, the energy dependence of the direct polarization potential is consistent with the breakup threshold anomaly (BTA) [21,22], while the fusion polarization potential follows the usual threshold anomaly (TA) [19,20]. Such TA, characterized by a rapid falling down of the imaginary strength of the fusion polarization potential at and below the Coulomb barrier, is consistent in this case with the fact that fusion channels are strongly suppressed below the barrier. The BTA, on the other hand, is associated to the weakly bound nature of the projectile, which can cause absorption stronger than usual into breakup (or other direct) channels around or even below the Coulomb barrier. This leads to a possible increase in the imaginary strength of the direct polarization potential for energies close and below the Coulomb barrier, followed by a drop to zero at some point when the energy is further lowered; these features partially characterize the BTA. Whereas attractive real parts were obtained for the fusion polarization potentials, an effective repulsive contribution was present in the direct polarization potentials. This is consistent with observations that, whereas in the case of strongly bound nuclei (where the TA holds) the real part of the potential shows an increase in attraction as the energy is lowered below the Coulomb barrier, the scattering of weakly bound nuclei shows a reduction of attraction [3]. It has been actually shown that the effects of breakup couplings can cause an effective repulsive contribution [23]. Since the ${}^6\text{He}$ projectile has an even weaker binding than ${}^6\text{Li}$ (0.98 vs 1.47 MeV), it should be interesting to investigate whether a similar threshold behavior is also present in the case of the ${}^6\text{He} + {}^{64}\text{Zn}$ system.

Section II briefly describes the formalism and the general form of the potentials used, while in Sec. III the obtained polarization potentials are presented and the respective predictions for elastic scattering, total reaction and fusion cross sections are shown. Section IV is devoted to discuss the energy behavior of both the total reaction cross sections and the extracted polarization potentials, as well as some effects related to the halo nature of ${}^6\text{He}$. Finally, a summary and the conclusions are given in Sec. V.

II. BRIEF DESCRIPTION OF THE FORMALISM

The model potential used here, defined within the general framework of the EOM [17,18] but containing important particularities, has been described in detail in Ref. [16]. Briefly, the potential is written as

$$U_{\text{TOT}} = V_{\text{bare}} + V_{\text{Coul}} - [iW_{\text{int}} + U_F + U_D], \quad (1)$$

where V_{Coul} is the Coulomb potential (with radius $r_C = 1.2$ fm) and W_{int} is a volume Woods-Saxon potential interior to the barrier whose depth, radius, and diffuseness are given by $W_0 = 50$ MeV, $r_0 = 1.0$ fm, and $a_0 = 0.2$ fm, respectively. The SPP [13] is used as the bare nuclear potential, V_{bare} , taking due account of the experimental nuclear density obtained for ${}^6\text{He}$ in Ref. [24].

U_F and U_D are complex polarization potentials which can be associated to couplings of the elastic channel with corresponding fusion and direct channels, respectively [25–27]. A volume Woods-Saxon (a derivative Woods-Saxon) shape is used for U_F (U_D), respectively, and, in order to keep the number of free parameters at a minimum, in each case the same radius and diffuseness are used for both, the respective real and imaginary parts. Thus, $U_{F,D}$ can be written as

$$\begin{aligned} U_F(r, E) &= V_F(r, E) + iW_F(r, E) \\ &= (V_{F0}(E) + iW_{F0}(E))f(r), \end{aligned} \quad (2)$$

$$\begin{aligned} U_D(r, E) &= V_D(r, E) + iW_D(r, E) \\ &= (V_{D0}(E) + iW_{D0}(E))f'(r), \end{aligned} \quad (3)$$

where $f(r) = 1/(1 + \exp[(r - R_F)/a_F])$ and $R_F = r_F(A_p^{1/3} + A_t^{1/3})$, being $A_{p,t}$ the mass number of the projectile (target), respectively. The reduced radius is taken as $r_F = 1.4$ fm while the respective diffuseness is fixed at $a_F = 0.43$ fm for all energies. These values have been used in similar descriptions of several systems [18,25–28] and did also give consistent results in the systematic study of medium mass targets with ${}^6\text{Li}$ projectiles [16]. In Eq. (3), $f'(r) = 4 \times EXP/(1 + EXP)^2$, $EXP = \exp[-(r - R_D)/a_D]$, $R_D = r_D(A_p^{1/3} + A_t^{1/3})$, where r_D is the reduced radius and a_D is the respective diffuseness.

To fix the values of r_D and a_D , a prescription introduced in Ref. [16] was used, whereby the elastic scattering angular distributions are reduced as shown in Fig. 1, where the abscissa, d , is the reduced distance of closest approach on a Rutherford trajectory, given by

$$\begin{aligned} D &= d(A_p^{1/3} + A_t^{1/3}) = \frac{1}{2}D_0 \left(1 + \frac{1}{\sin(\theta_{\text{c.m.}}/2)} \right) \\ \text{with } D_0 &= \frac{Z_p Z_t e^2}{E_{\text{c.m.}}} \end{aligned} \quad (4)$$

The solid black curve in Fig. 1 corresponds to a fit of the three-parameter nonlinear function $g(x) = a(1 + \exp[-k(x - x_c)])^{-1}$. This is just an auxiliary function having no physical meaning; it has the property that $g(1.51) = 0.25$ and this defines the strong absorption distance for the present system as $d_S = 1.51$ fm. This is also the value assumed for r_D [16], i.e., $r_D = 1.51$ fm. As for the dotted magenta curve, it is a

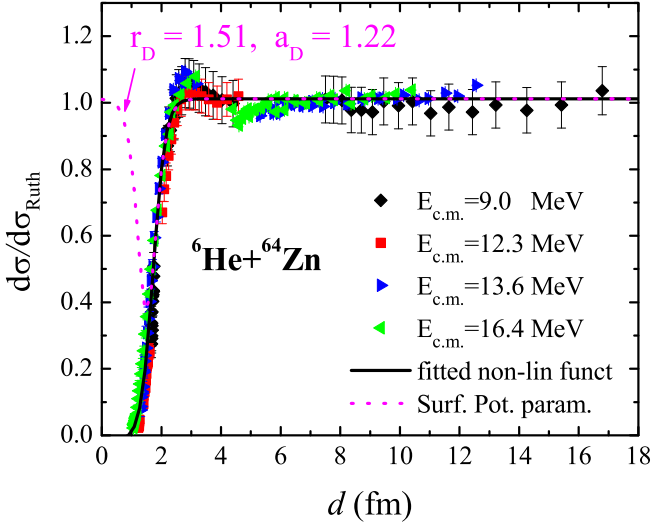


FIG. 1. Plot of $d\sigma/d\sigma_{\text{Ruth}}$ vs d for the ${}^6\text{He} + {}^{64}\text{Zn}$ elastic scattering data of Refs. [8,10]. The meaning of the curves is explained in the text.

plot of the two-parameter function $1 - \gamma f'(r)$, where $f'(r)$ is the derivative Woods-Saxon form factor defined in connection with Eq. (3). Fixing r_D as above leaves only the parameter a_D in $f'(r)$. The two parameters γ and a_D are fitted so that the right wing of the dotted curve matches the solid curve, which gives the value $a_D = 1.22$ fm for the diffuseness of the direct polarization potential U_D .

Within the EOM, the fusion cross section is obtained from the absorption in both W_{int} , which accounts for absorption inside the barrier, and W_F , which incorporates absorption under the barrier. The corresponding expression is [17]

$$\sigma_{\text{fus}} = \frac{2}{\hbar v} \langle \chi^{(+)} | W_{\text{int}} + W_F | \chi^{(+)} \rangle, \quad (5)$$

where v is the relative velocity and $\chi^{(+)}$ is the distorted wave function that satisfies the Schrödinger equation corresponding to the full optical potential of Eq. (1).

Summarizing, an optical potential has been defined having four free parameters: the real and imaginary strengths of the polarization potentials, (V_{D0}, W_{D0}) and (V_{F0}, W_{F0}) . These parameters will be varied to simultaneously fit the respective fusion and elastic scattering data. In addition, dispersive potentials will be searched for, i.e., potentials satisfying the dispersion relation, which is written as [19,20]

$$V(E) = V(E_S) + \frac{E - E_S}{\pi} P \int_0^\infty \frac{W(E')}{(E' - E_S)(E' - E)} dE'. \quad (6)$$

In expression (6), P stands for the principal value and $V(E_S)$ is the value of $V(E)$ evaluated at some reference energy $E = E_S$. Considering the particular functional forms of the polarization potentials [Eqs. (2) and (3)], Eq. (6) reduces to a relation between the respective potential strengths. In general, the constraint of having dispersive potentials amounted to make only minor adjustments to the values obtained from the automatic parameter optimization.

TABLE I. Strengths obtained for the polarization potentials at the different experimental energies.

$E_{\text{c.m.}}$ (MeV)	V_{D0} (MeV)	W_{D0} (MeV)	V_{F0} (MeV)	W_{F0} (MeV)
9.0	-0.43	0.3	3.9	2.5
12.3	-0.54	0.52	4.0	3.3
13.6	-0.60	0.2	2.0	3.3
16.4	-0.64	0.27	1.8	4.2

III. RESULTS

The optical model calculations were carried out using the code FRESKO and its search version, SFRESKO [29]. For each energy E_i , where an experimental angular distribution $d\sigma/d\Omega(\theta, E_i)$ has been measured, a corresponding value of $\sigma_{\text{fus}}(E_i)$ was obtained, by interpolation of the respective experimental values. A simultaneous fit of $d\sigma/d\Omega(\theta, E_i)$ and $\sigma_{\text{fus}}(E_i)$ was performed in the usual way, by minimizing the corresponding value of χ^2/N . The validity of the dispersion relation was checked, separately for the direct and the fusion polarization parts of the potential, and additional adjustments to the parameters were made when needed. The final strength values of the polarization potentials are shown in Table I.

Figure 2 shows the measured elastic scattering angular distributions along with the curves calculated from the optical model potentials obtained in the present work. Reasonably good descriptions of the data can be observed, which are actually similar to those obtained in the original work of Ref. [10]. The present potential, however, has the imposed additional constraints of reproducing the fusion cross sections and satisfying the dispersion relation.

The predicted fusion cross sections are compared to the respective experimental quantities in Fig. 3, where the corresponding values of the total reaction cross sections also are shown. The fusion predictions at the two lowest energies perfectly match the experimental values and those for the two

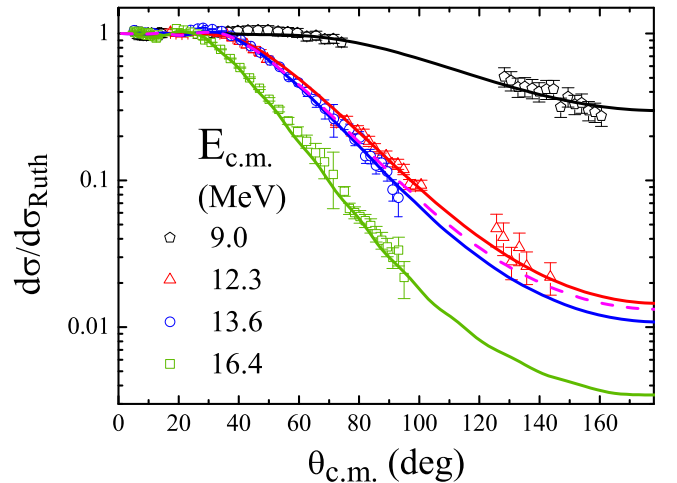


FIG. 2. Symbols: elastic scattering angular distributions reported in [8,10]; the solid curves are the results of present fits and the dashed curve will be explained in Sec. IV B.

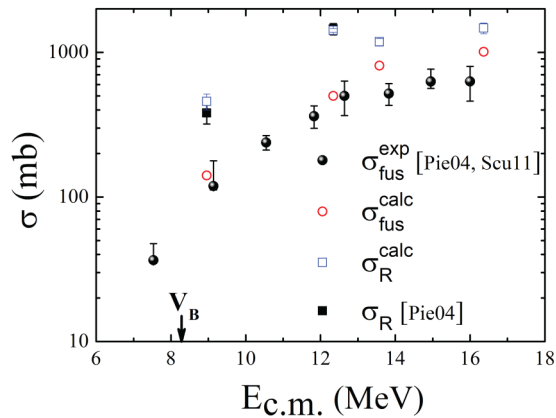


FIG. 3. Calculated total reaction and fusion cross sections compared to the experimental values. Open symbols show the present theoretical results while filled symbols represent the reported data. (Pie04: [8]; Scu11: [9]).

highest energies slightly overpredict the data, but they are still consistent, however marginally, with the reported error bars. It is worth mentioning that the reported values of $\sigma_{\text{fus}}^{\text{exp}}$ involve the subtraction of a substantial nonfusion yield of ^{65}Zn whose contribution was estimated by means of a statistical model calculation [8,9]. Additional fusion measurements would be needed to clarify the slight discrepancy with our calculated results.

On the other hand, the predicted values for the total reaction cross sections are consistent with the respective values reported for the two lowest energies in Ref. [8]. No total reaction cross sections have been reported earlier for the two highest energies.

Summarizing, the potentials obtained within the framework of the EOM in the present work do provide a simultaneous description of the elastic scattering [8,10] and fusion [8,9] data reported for the halo system $^6\text{He} + ^{64}\text{Zn}$. Some consequences and further discussion will be given in next section.

IV. DISCUSSION

A. A transition in the direct reaction mechanisms

One can notice in Fig. 3 that σ_R presents a local maximum at ≈ 12.3 MeV; in particular, the respective experimental point shows a σ_R value larger than that corresponding to the next higher energy, 13.6 MeV. Even considering respective uncertainties, included in Fig. 3, such a behavior can be clearly pointed out (see Sec. IV B for further details). It may be mentioned that, by doing calculations with different optical potentials that reproduce well the elastic scattering angular distributions, realistic uncertainties were assigned to all present values of σ_R . One of these optical potentials was in fact the one used in the original experimental work of Ref. [10].

The above local maximum also can be corroborated by looking at the experimental cross sections for α particle yields in $^6\text{He} + ^{64}\text{Zn}$ reactions, which were measured in Refs. [8,9] and also reported in Ref. [10]. In the latest reference, the

TABLE II. Comparison of the direct reaction cross sections estimated in the present work, σ_{dir} , with the integrated α particle cross sections, σ_{α} , obtained in the present work from the measurements of Refs. [8–10].

$E_{\text{c.m.}}$ (MeV)	σ_{dir} (mb)	σ_{α} (mb)
9.0	339 ± 83	366 ± 23
12.3	969 ± 109	994 ± 8
13.6	663 ± 111	743 ± 56
16.4	842 ± 211	974 ± 17

authors concluded that such α particles stem mainly from nonelastic breakup mechanisms involving the transfer or absorption of the loosely bound neutrons by the target. As a matter of fact, most of the corresponding direct reaction channels are expected to be accounted for by these inclusive α yields. We have integrated the α particle angular distributions of Refs. [8–10] (see Sec. IV B for details) to get respective cross sections σ_{α} , which are presented in Table II along with the direct reaction cross sections estimated in the present work as $\sigma_{\text{dir}} = \sigma_R^{\text{calc}} - \sigma_{\text{fus}}^{\text{exp}}$ (see Fig. 3).

One can see from Table II that σ_{dir} and σ_{α} are consistent with each other and, in addition, they both show a local maximum at the energy 12.3 MeV. In other words, the local maximum observed in σ_R , which was obtained from the present EOM analyses of elastic scattering angular distributions, is consistent with the local maximum obtained from the experimental α particle yields. Thus, such maximum must be originated by some kind of transition in the involved direct reaction mechanisms.

A local enhancement in the total reaction cross sections has been observed in measurements with ^6He and ^9Li projectiles on a ^{28}Si target [30]. Such enhancement was ascribed to a transition in the rearrangement of the loosely bound neutrons in the projectile, which may appear with a high probability between the surfaces of both reacting nuclei, thus enhancing strongly the mutual attraction and leading to an increase in the total reaction cross section. The probability of neutron rearrangement would depend on the ratio between the relative speed of colliding nuclei, v_r , and the average speed of outer neutrons in the projectile, v_n . For a low value of $\gamma = v_r/v_n$, the neutrons can make several turns around the nuclear cores of colliding nuclei during the passing time, when such nuclei are close to each other; in this case, the neutrons may have enough time to interact with the target and actually affect the reaction cross section. Penionzhkevich *et al.* [30] interpret the local maximum as resulting from a transition between an adiabatic and a nonadiabatic rearrangement of the neutrons.

By using the approximations described in Ref. [30], a ratio $\gamma \approx 0.47$ is estimated corresponding to the energy 12.3 MeV in the present system. For the reactions analyzed in Ref. [30], the enhancement was especially significant in the energy range where $\gamma \approx 1$. In order to corroborate whether the above mechanism may be responsible for the local maximum observed in the present system, it would be interesting to have proper theoretical calculations describing the time evolution of the loosely bound neutrons of ^6He in collisions with ^{64}Zn .

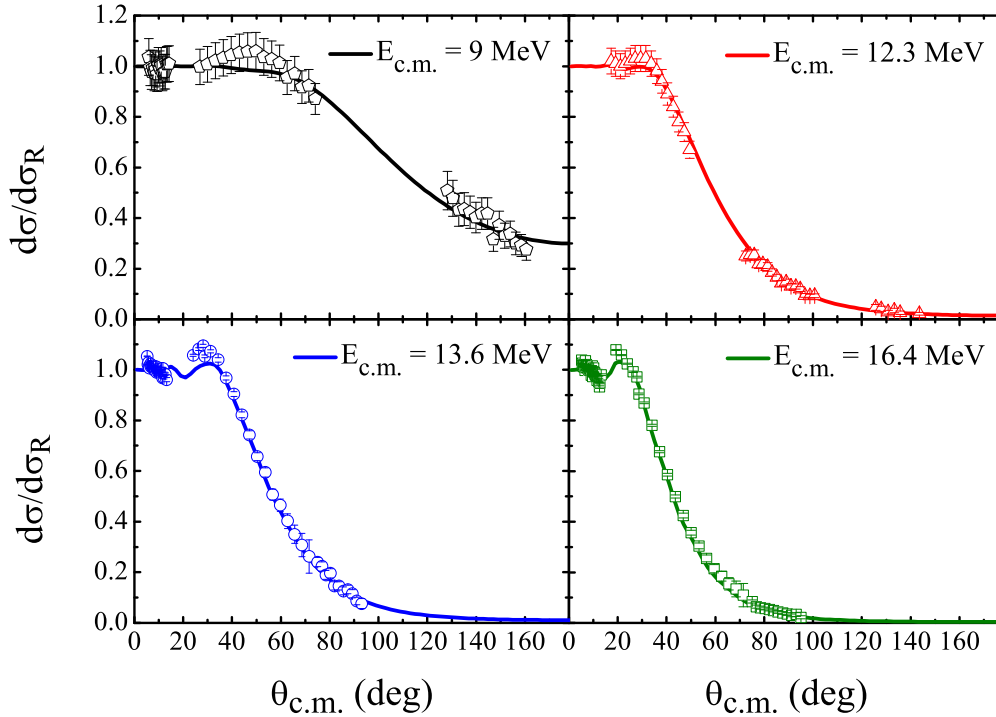


FIG. 4. The elastic scattering angular distributions from Fig. 2, but plotted in linear scale (data from [8,10]).

Such local maximum, which is yet to be understood, will be seen in Sec. IV C that leads to a threshold anomaly which shows a strikingly irregular behavior.

B. About robustness of previous results

Given the importance of the above results, it is worth mentioning a few supporting words. First, the vertical scale in Fig. 2 was chosen so that the complete theoretical angular distributions could be plotted, which may leave the impression of an apparently important lack of large angle data for the two highest energies. One might thus wonder whether an actual measurement of cross sections at those large angles may change the values of extracted total reaction cross sections and perhaps discard the claimed local maximum.

This is actually not a real issue, because the smallest measured values of $d\sigma/d\sigma_{\text{Ruth}}$ are already at the low levels of 0.08 and 0.02 for $E_{\text{c.m.}}$ values of 13.6 and 16.4 MeV, respectively. No significant effect should be obtained from the even smaller cross sections that could be expected at larger angles. To make this more evident, the same angular distributions have been plotted in Fig. 4, but using a linear scale. For the two largest energies, the observed trend of the data clearly indicates that any possible experimental points lying in the angular region above 95° most probably will not have any significant influence on the corresponding fitted curves and therefore on the respective values of σ_R^{calc} .

To further stress the above point, it was checked that the extracted total reaction cross sections are mainly sensitive to the angular region where data actually exist. The case of the angular distribution corresponding to $E_{\text{c.m.}} = 13.6$ MeV is illustrated here; this energy is actually the most critical

one to define the decreasing part of the mentioned local maximum in σ_R^{calc} . It has been shown that, within the EOM framework, angular distributions at large angles are mainly sensitive to the fusion polarization potential [31]. To simulate a possible change of the angular distribution in the region of large angles, the respective value of W_{F0} was increased from 3.3 (see Table I) up to 4.5 MeV (a decrease of W_{F0} would not be consistent with the dispersion relation discussed in Sec. IV C). As a result, σ_R^{calc} changed by a negligible 0.16%, but in the decreasing direction, i.e., in the direction that in principle would help elucidate even better the local maximum. The fusion cross section did increase, but only by 2%, a rather insignificant change too. The elastic scattering angular distribution, on the other hand, suffered a small deviation upwards mainly in the large angle region, as seen in the dashed magenta curve of Fig. 2. Therefore, σ_R^{calc} is not sensitive even to fairly significant changes in the elastic scattering angular distribution at the largest angles.

Summarizing, it is clear that the extracted values of the total reaction cross sections reliably and unambiguously stem from the published data. The respective uncertainties, assigned in the usual way (see Sec. IV A), can also be considered quite realistic. The robustness of the observed local maximum in σ_R^{calc} is thus verified.

The procedure to extract the values of σ_α reported in Table II deserves special attention too. The corresponding α particle angular distributions are presented in Fig. 5 [8–10]. The blue solid curves represent the IAV model calculations reported by Fernández-García *et al.* [10], while the red dotted curves are the angular distributions that were actually integrated to obtain σ_α . These later curves were obtained by doing a linear interpolation for internal points (two internal

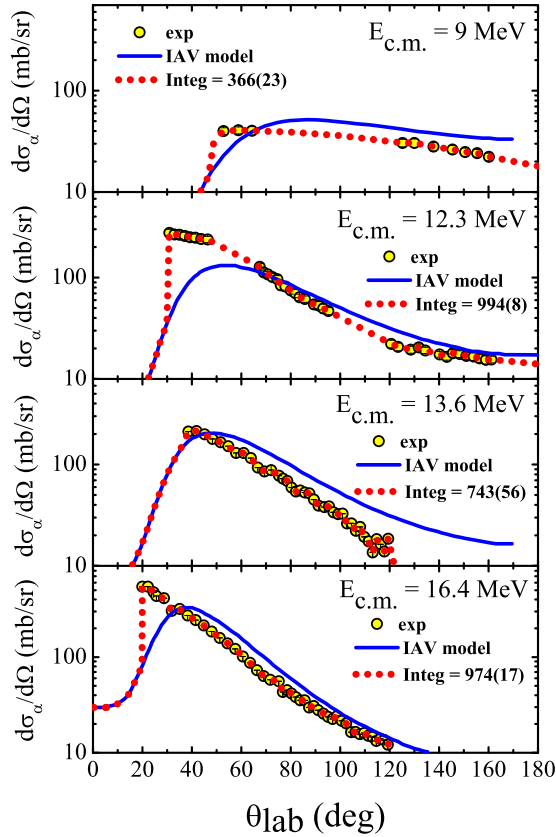


FIG. 5. α particle angular distributions integrated to obtain σ_α (data from [8–10]). Curves are described in the text.

points were added artificially in the case of $E_{c.m.} = 9$ MeV and using the blue curves as a guide to extrapolate.

For large angles, the trend of the data and the comparison with the respective trend of the IAV curves reasonably define the most probable extrapolation. The left-hand side extrapolation is somewhat more uncertain, but the falling trend of the IAV curves toward small angles was always followed. The number resulting from the integration of the left tail in each case, below the lowest measured angle, was assigned as the respective uncertainty reported for σ_α in Table II.

Independently of the extrapolation criterion chosen, a careful visual comparison of the experimental α particle angular distributions corresponding to 12.3 and 13.6 MeV, clearly indicates that the former one encloses a larger area, i.e., it corresponds to a bigger integrated cross section, thus corroborating the presence of a maximum in σ_α . The fact that there is an almost perfect coincidence between the σ_{dir} and σ_α columns of Table II does actually add trustability to the described extrapolation procedure.

C. Threshold anomalies

In Fig. 6 the variation with energy of the polarization-potential strengths obtained in the present work (see Table I) is displayed. The left panel refers to the fusion polarization potential, U_F . The strengths corresponding to the imaginary part, W_{F0} , can be approximated by the solid straight lines shown. The threshold energies where the inclined straight lines of

Fig. 6 have strength zero are obtained as done in Ref. [16], by finding the value at which the linear fit to the quantity $S_{F,D} = \sqrt{E\sigma_{F,D}}$ reaches zero [32]. Here, σ_F represents the experimental fusion cross section, σ_{fus} , and $\sigma_D = \sigma_R - \sigma_{fus}$. This procedure was carried out as illustrated in Fig. 7, yielding a value of 6 MeV for both thresholds.

The piecewise linear approximation to W_{F0} is then used in the dispersion relation, Eq. (6), to obtain the dashed curve in the lower left panel. This later curve is consistent with the points extracted for V_{F0} from the optimization procedure, within error bars. Such error bars were obtained as described in Ref. [16], by finding extreme strength values for which an acceptable description of the corresponding angular distribution can still be obtained.

Likewise, the right panel of Fig. 6 refers to the direct reaction polarization potential, U_D . The piecewise linear approximation in the upper part and the dashed curve in the lower part have similar meanings as explained above for U_F . It is noticed in this case also that the dashed curve is consistent with the respective points, within uncertainties.

The previous paragraphs can be summarized by saying that the polarization potentials obtained in the present work do satisfy the dispersion relation. The particular energy behavior in each case can be further discussed within the context of the so-called threshold anomalies.

At first sight, the energy behavior of the fusion polarization potential seems very similar to that observed for ${}^6\text{Li}$ induced reactions [16], as briefly described in Sec. I. Similar to the ${}^6\text{Li}$ -projectile systems, an apparently typical TA behavior is observed for U_F . One can see in Fig. 6 that an attractive real part is obtained and, besides, there is a rapid falling down of the imaginary strength below the energy $E_{th} \approx 9.5$ MeV. This energy, however, is in the present case substantially shifted up with respect to the barrier height. Indeed, from the SPP used in the present work one gets the barrier parameters $V_B = 8.28$ MeV, $R_B = 9.66$ fm, so the shift amounts to $\approx +1.22$ MeV. This result may need to be corroborated by further measurements including finer energy steps but, if confirmed, it would indicate that fusion channels become strongly suppressed in the present system even at energies which are more than 1 MeV above the barrier. Consistent with this, one can easily estimate from Fig. 3 and Table II that, at 9 MeV, the fusion cross section amounts to only $\approx 32\%$ of σ_α .

As for the energy variation of the direct-reaction polarization potential, U_D , the behavior observed in the right panel of Fig. 6 is also qualitatively similar to that observed for the ${}^6\text{Li}$ induced systems of Ref. [16], which follow the BTA. However, in contrast to the latter systems, where W_{D0} shows a maximum at an energy E_{max} which is at or below the barrier, in the present case the corresponding value of E_{max} (≈ 12 MeV) is strikingly high, about 45% above V_B . Nevertheless, it is also remarked that negative real parts are obtained for U_D , implying a repulsive effective contribution of the direct polarization potential. This feature has been seen to characterize the BTA observed in many systems and has been actually related to the effect of breakup couplings [23]. We conclude thus that the present data yield a direct-reaction polarization potential which follows a behavior of the BTA type, but with a strikingly large value of E_{max} .

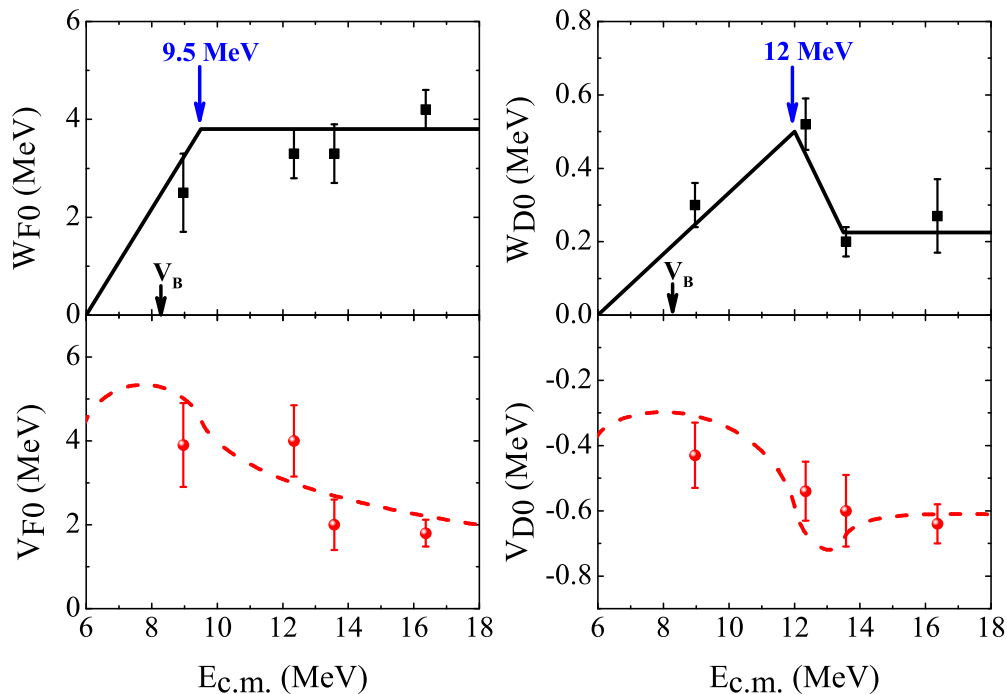


FIG. 6. (Left) Energy dependence of the real (down) and imaginary (up) strengths of the fusion polarization potential. (Right) The same but for the direct-reaction polarization potential. The arrows on the horizontal axis indicate the barrier height.

The prominently large value of W_{D0} at $E_{\max} \approx 12$ MeV is correlated with the observed local maximum in σ_R commented on in the previous subsections; in other words, the presence of such local maximum leads to the unusual BTA-type behavior described above. A possible mechanism behind this local maximum also was commented there, although it was pointed out that more theoretical work is needed. The origin of the observed up shifts in E_{th} and E_{\max} , with respect to observations for other systems, could probably be attributed to the halo character of ${}^6\text{He}$, but this is yet to be understood.

It is worth comparing with results from a similar analysis for data corresponding to the ${}^6\text{He} + {}^{209}\text{Bi}$ system [33–35], which were analyzed within the EOM in Ref. [26]. The authors concluded that the fusion potential exhibits a threshold anomaly very similar to that observed for tightly bound projectiles. The value of E_{th} is in this case 18.5 MeV, slightly lower than the respective SPP barrier (19.06 MeV). The larger value of E_{th}/V_B for the present ${}^{64}\text{Zn}$ target may be due to the corresponding lower Coulomb repulsion in this later case. This may facilitate the halo tail to get closer to the target, thus allowing direct-channel dominance over fusion to set up at higher energies relative to the Coulomb barrier. As for the direct reaction potential, no threshold anomaly was observed for the case of the ${}^{209}\text{Bi}$ target [26]. However, the maximum energy analyzed in that case was only 12% above the respective Coulomb barrier, far lower with respect to the barrier than the value $E_{\max} \approx 1.45V_B$ obtained in the present case. Higher energy measurements for ${}^6\text{He} + {}^{209}\text{Bi}$ would be needed in order to confirm (or discard) the presence of a similar BTA behavior in this heavier system.

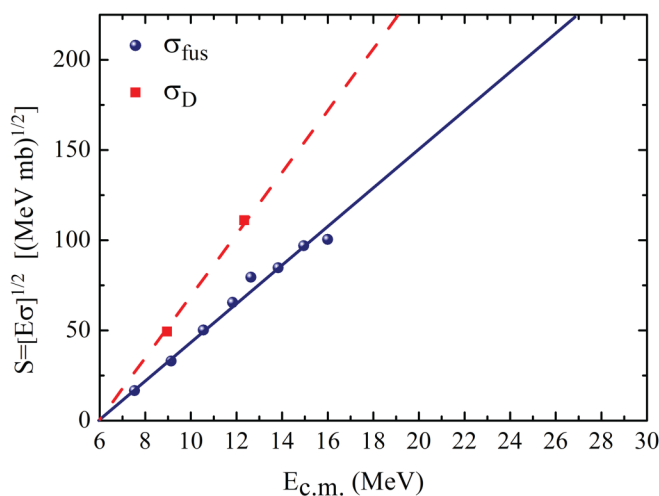


FIG. 7. Straight line fits to $S_{F,D}$ for data corresponding to the ${}^6\text{He} + {}^{64}\text{Zn}$ system [8,9]. Threshold energies are 6 MeV in both cases.

D. Halo features in ${}^6\text{He} + {}^{64}\text{Zn}$

The values obtained above for the parameters r_D , a_D of U_D (1.51, 1.22) fm can be compared to those obtained in Ref. [16] for ${}^6\text{Li}$ on the same target (1.6, 0.85) fm. It may be remarked that the same prescription introduced in such reference to phenomenologically extract these parameters out from the elastic scattering data, was also used in the present work. Whereas for the halo nucleus ${}^6\text{He}$ the radius is slightly lower (by 6%) than for ${}^6\text{Li}$, the corresponding diffuseness is considerably higher (by 44%). This is actually consistent with

the conclusions of Ref. [36] that neutron-halo nuclei reacting on medium mass targets present a distinctively extended direct-interaction region as compared to stable weakly-bound or tightly bound projectiles.

Indeed, the critical interaction distance d_l , where the nuclear interaction between the colliding nuclei begins to be felt, was deduced for many systems in Ref. [36]. As discussed there, the difference of d_l with the strong interaction distance, $\Delta = d_l - d_s$, corresponds to a region of predominance for direct reaction processes. The systematics of Ref. [36] showed that Δ progressively increases when going from tightly bound, through stable weakly bound, to halo projectiles. For the particular case of (${}^6\text{He}$, ${}^6\text{Li}$) + ${}^{64}\text{Zn}$, it can be seen that the respective values of Δ differ by 48%, close to the 44% difference in diffuseness mentioned above. Reference [36] deals only with medium mass targets but similar conclusions also were obtained from analyzes of several projectiles with a heavier target [37], which indicates that the relatively higher values of Δ for ${}^6\text{He}$ are actually due to the halo character of this projectile, independent of the target.

Therefore, the extended region for direct interactions with ${}^6\text{He}$ is explained in the present prescription by a large diffuseness of the direct polarization potential. This long-range component of the potential would reflect dynamic effects of the long tail of the neutron-halo wave function and could be associated to the large transfer/breakup probabilities observed experimentally (see last column of Table II), as well as to the effect of a large value of the respective Coulomb dipole polarizability. More theoretical work is needed in order to fully understand the detailed origin of this long-range component.

The halo effects in the present system also can be tested from an analysis of the total reaction cross sections, σ_R , extracted from the optical model calculations and presented in Fig. 3 for the four energies measured. It has been shown [38] that the σ_R results obtained for many systems with a ${}^6\text{He}$ projectile present a systematic behavior that can be contrasted with respective results for the corresponding core nucleus, ${}^4\text{He}$. The observed differences between the two projectiles can be interpreted in terms of the halo feature.

Basically, in Ref. [38] the values of σ_R were reduced by dividing them by the factor $\eta = (A_p^{1/3} + A_t^{1/3})^2$ while the energies were in turn divided by $\xi = Z_p Z_t / (A_p^{1/3} + A_t^{1/3})$ to obtain reduced energies. A plot of σ_{Red} vs E_{Red} for nine systems having ${}^6\text{He}$ as projectile, giving a total of 28 points, showed that the respective values followed a common trajectory. A similar plot corresponding to ${}^4\text{He}$ projectiles on eight different targets (a total of 43 points) did also follow a common trajectory, this one lying below the previous one. Both trajectories were nicely parametrized with the expression

$$\sigma_{\text{Red}}^W = \frac{\epsilon_0 r_{0b}^2}{2E_{\text{Red}}} \ln \left\{ 1 + \exp \left[\frac{2\pi}{\epsilon_0} (E_{\text{Red}} - V_{\text{Red}}) \right] \right\}, \quad (7)$$

where $E_{\text{Red}} = E_{\text{c.m.}}/\xi$ is the reduced energy, $\epsilon_0 = \hbar\omega_0/\xi$ is the reduced barrier-curvature parameter, $r_{0b} = R_0/\eta^{(1/2)}$ is the reduced radius, $V_{\text{Red}} = V_0/\xi$ is the reduced barrier height, and $\sigma_{\text{Red}}^W = \sigma^W/\eta$ is the reduced cross section corresponding to Wong's formula [39]. For ${}^6\text{He}$ (${}^4\text{He}$), the best-fit values

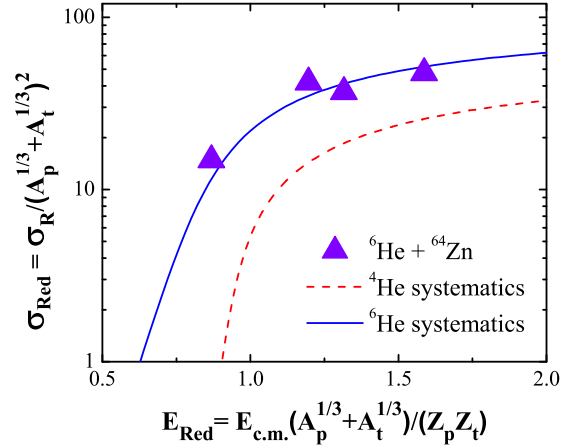


FIG. 8. Reduced total reaction cross sections for ${}^6\text{He} + {}^{64}\text{Zn}$. The curves are explained in the text.

of V_{Red} , r_{0b} , ϵ_0 were 0.780, 1.79, 0.43 (0.913, 1.39, 0.175), respectively.

The two curves obtained by replacing the above values of reduced parameters in Eq. (7) are plotted in Fig. 8, along with the reduced values of the total reaction cross sections of Fig. 3. One can see that these latter values do follow the trend of the ${}^6\text{He}$ -projectile curve, keeping the previously observed striking enhancement with respect to the curve corresponding to ${}^4\text{He}$ projectiles. As discussed in Ref. [38], this enhancement can be interpreted as being the consequence of both, a static halo effect directly related to the extended size of the halo nucleus, and a dynamic halo effect related to an increased diffuseness of the absorption in l space.

Although the two lowest-energy experimental data of Fig. 8 were also analyzed within the same context in Ref. [38], the σ_R values in that case were obtained by using different optical potentials [8]. The present analysis includes in addition two higher energy data, from Ref. [10], and uses the present EOM potentials to extract all σ_R values. The conclusion of combined static and dynamic halo effects is thus shown to be valid for ${}^6\text{He} + {}^{64}\text{Zn}$ independently of the optical potential shape (as long as the elastic scattering data are well reproduced) and, in particular, it holds also for the two newer experimental data.

V. SUMMARY AND CONCLUSIONS

The data reported in the literature for elastic scattering and fusion of the neutron halo system ${}^6\text{He} + {}^{64}\text{Zn}$ were analyzed within the framework of the extended optical model. The SPP was used as bare potential and dynamic polarization potentials U_F and U_D were obtained, which can be associated to fusion and direct reaction couplings, respectively. Following the method of Ref. [16], a volume Woods-Saxon shape was used for U_F while U_D had a derivative Woods-Saxon shape; the respective strengths, a total of only four free parameters, were fitted to the data for each energy, watching always the validity of the dispersion relation. A good description of the elastic scattering angular distributions and the fusion excitation function was achieved.

A substantially large value was used for the diffuseness, a_D , of the direct reaction polarization potential, U_D . Such value, obtained from the elastic scattering data through a prescription previously introduced [16], is a clear indication of the presence of a long range absorption and simulates an extended region of direct reaction dominance, which is characteristic of halo systems [36].

An unexpected local maximum was uncovered in the total reaction cross sections which was shown to be correlated with respective measurements of inclusive α particles produced in direct reactions. This indicates some kind of transition in the involved direct reaction processes and a possible mechanism responsible for it was discussed.

The energy dependence of U_F followed a trend consistent with the threshold anomaly but the threshold energy E_{th} was noticeably above the barrier, by ≈ 1.22 MeV. This is in contrast to the typical behavior observed for instance for ${}^6\text{Li}$ -induced systems [16], where E_{th} is closer to the barrier. Likewise, $U_D(E)$ was consistent with the qualitative behavior typical of the breakup threshold anomaly, but the peak energy E_{max} was in this case strikingly high above the barrier, by about 3.7 MeV. For other weakly bound systems analyzed previously [16], E_{max} is close or even below the barrier. The same mechanism behind the local maximum mentioned above must be responsible for the observed BTA. Such atypical behavior of E_{th} and E_{max} is probably related to the halo character of ${}^6\text{He}$, but more work is needed in order to be fully understood. In particular, further measurements would be convenient to corroborate the present results.

The total reaction cross sections obtained from the optical model calculations were properly reduced and plotted versus respective reduced energies. The corresponding points nicely

followed the trajectory obtained previously from a systematics of many ${}^6\text{He}$ -induced systems, which is considerably enhanced with respect to the similar trajectory corresponding to ${}^4\text{He}$ -induced reactions [38]. These results corroborate the presence of static and dynamic halo effects in the ${}^6\text{He} + {}^{64}\text{Zn}$ system.

In summary, for the present system it was possible to find dispersive polarization potentials for both the direct-reaction and the fusion parts, which simultaneously described the respective elastic scattering and fusion data. These findings can be globally enclosed within the results of the extensive work done previously in the framework of the EOM. Both tightly bound [25,40,41] and weakly bound [16,26,28,42–45] systems have been successfully analyzed using the EOM. The fact that $U_D(E)$ presents a behavior of the BTA type while $U_F(E)$ is more similar to the usual TA behavior, has been also observed for other weakly bound systems [16,27,28,42–44,46]. Different from all previous results, however, the present halo system exhibits an unusually high value of E_{th} , the threshold energy related to $W_{F0}(E)$, as well as a strikingly high value of the energy E_{max} at which the maximum in W_{D0} occurs. This latter result could be indicative of some non conventional reaction mechanism that sets up at the energy E_{max} , a possibility for it was discussed but this is yet to be understood. It would be desirable to have further measurements including additional energies in ${}^6\text{He} + {}^{64}\text{Zn}$ and also with other ${}^6\text{He}$ -projectile systems, which may corroborate the present results.

ACKNOWLEDGMENTS

This work has been partially supported by CONACYT (México), under Grant No. CB-01-254619.

-
- [1] N. Keeley, R. Raabe, N. Alamanos, and J. L. Sida, *Prog. Part. Nucl. Phys.* **59**, 579 (2007).
- [2] N. Keeley, N. Alamanos, K. W. Kemper, and K. Rusek, *Prog. Part. Nucl. Phys.* **63**, 396 (2009).
- [3] L. F. Canto, P. R. S. Gomes, R. Donangelo, J. Lubian, and M. S. Hussein, *Phys. Rep.* **596**, 1 (2015).
- [4] J. J. Kolata, V. Guimarães, and E. F. Aguilera, *Eur. Phys. J. A* **52**, 123 (2016).
- [5] I. Tanihata, H. Hamagaki, O. Hashimoto, S. Nagamiya, Y. Shida, N. Yoshikawa, O. Yamakawa, K. Sugimoto, T. Kobayashi, D. E. Greiner, N. Takahashi, and Y. Nojiri, *Phys. Lett. B* **160**, 380 (1985).
- [6] J. M. Bang, B. V. Danilin, V. D. Efros, J. S. Vaagen, M. V. Zhukov, and I. J. Thompson, *Phys. Rep.* **264**, 27 (1996).
- [7] A. Di Pietro, P. Figuera, F. Amorini, C. Angulo, G. Cardella, S. Cherubini, T. Davinson, D. Leanza, J. Lu, H. Mahmud, M. Milin, A. Musumarra, A. Ninane, M. Papa, M. G. Pellegriti, R. Raabe, F. Rizzo, C. Ruiz, A. C. Shotton, N. Soic, and S. Tudisco, *Europhys. Lett.* **64**, 309 (2003).
- [8] A. Di Pietro, P. Figuera, F. Amorini, C. Angulo, G. Cardella, S. Cherubini, T. Davinson, D. Leanza, J. Lu, H. Mahmud, M. Milin, A. Musumarra, A. Ninane, M. Papa, M. G. Pellegriti, R. Raabe, F. Rizzo, C. Ruiz, A. C. Shotton, N. Soić, S. Tudisco *et al.*, *Phys. Rev. C* **69**, 044613 (2004).
- [9] V. Scuderi, A. Di Pietro, P. Figuera, M. Fisichella, F. Amorini, C. Angulo, G. Cardella, E. Casarejos, M. Lattuada, M. Milin, A. Musumarra, M. Papa, M. G. Pellegriti, R. Raabe, F. Rizzo, N. Skukan, D. Torresi, and M. Zadro, *Phys. Rev. C* **84**, 064604 (2011).
- [10] J. P. Fernández-García, A. Di Pietro, P. Figuera, J. Gómez-Camacho, M. Lattuada, J. Lei, A. M. Moro, M. Rodríguez-Gallardo, and V. Scuderi, *Phys. Rev. C* **99**, 054605 (2019).
- [11] K. Hagino, N. Rowley, and A. T. Kruppa, *Comput. Phys. Commun.* **123**, 143 (1999).
- [12] E. Crema, P. R. S. Gomes, and L. C. Chamon, *Phys. Rev. C* **75**, 037601 (2007).
- [13] L. C. Chamon, B. V. Carlson, L. R. Gasques, D. Pereira, C. De Conti, M. A. G. Alvarez, M. S. Hussein, M. A. Cândido Ribeiro, E. S. Rossi, Jr., and C. P. Silva, *Phys. Rev. C* **66**, 014610 (2002).
- [14] E. Crema, L. C. Chamon, and P. R. S. Gomes, *Phys. Rev. C* **72**, 034610 (2005).
- [15] K. Hagino, T. Takeki, A. B. Balantekin, and N. Takigawa, *Phys. Rev. C* **71**, 044612 (2005).
- [16] F. Torabi, E. F. Aguilera, O. N. Ghodsi, and A. Gómez-Camacho, *Nucl. Phys. A* **994**, 121661 (2020).

- [17] T. Udagawa and T. Tamura, *Phys. Rev. C* **29**, 1922 (1984).
- [18] T. Udagawa, B. T. Kim, and T. Tamura, *Phys. Rev. C* **32**, 124 (1985).
- [19] M. A. Nagarajan, C. C. Mahaux, and G. R. Satchler, *Phys. Rev. Lett.* **54**, 1136 (1985).
- [20] C. C. Mahaux, H. Ngô, and G. R. Satchler, *Nucl. Phys. A* **449**, 354 (1986).
- [21] P. R. S. Gomes, I. Padron, J. O. Fernández Niello, G. V. Martí, M. D. Rodríguez, O. A. Capurro, A. J. Pacheco, J. E. Testoni, A. Arazi, J. Lubian, R. M. Anjos, L. C. Chamon, E. Crema, and M. S. Hussein, *J. Phys. G* **31**, S1669 (2005).
- [22] M. S. Hussein, P. R. S. Gomes, J. Lubian, and L. C. Chamon, *Phys. Rev. C* **73**, 044610 (2006).
- [23] J. Lubian, T. Correa, P. R. S. Gomes, and L. F. Canto, *Phys. Rev. C* **78**, 064615 (2008).
- [24] L. R. Gasques, L. C. Chamon, D. Pereira, V. Guimarães, A. Lepine-Szilý, M. A. G. Alvarez, E. S. Rossi, Jr., C. P. Silva, B. V. Carlson, J. J. Kolata, L. Lamm, D. Peterson, P. Santi, S. Vincent, P. A. De Young, and G. Peaslee, *Phys. Rev. C* **67**, 024602 (2003).
- [25] B. T. Kim, W. Y. So, S. W. Hong, and T. Udagawa, *Phys. Rev. C* **65**, 044607 (2002).
- [26] B. T. Kim, W. Y. So, S. W. Hong, and T. Udagawa, *Phys. Rev. C* **65**, 044616 (2002).
- [27] W. Y. So, T. Udagawa, K. S. Kim, S. W. Hong, and B. T. Kim, *Phys. Rev. C* **75**, 024610 (2007).
- [28] W. Y. So, T. Udagawa, K. S. Kim, S. W. Hong, and B. T. Kim, *Phys. Rev. C* **81**, 047604 (2010).
- [29] Ian J. Thompson, *Comput. Phys. Rep.* **7**, 167 (1988).
- [30] Yu. E. Penionzhkevich, Yu. G. Sobolev, V. V. Samarin, and M. A. Naumenko, *Phys. At. Nucl.* **80**, 928 (2017).
- [31] E. F. Aguilera and F. Torabi, *J. Phys.: Conf. Ser.* **1610**, 012001 (2020).
- [32] P. H. Stelson, H. J. Kim, M. Beckerman, D. Shapira, and R. L. Robinson, *Phys. Rev. C* **41**, 1584 (1990).
- [33] J. J. Kolata, V. Guimarães, D. Peterson, P. Santi, R. White-Stevens, P. A. DeYoung, G. F. Peaslee, B. Hughey, B. Atalla, M. Kern, P. L. Jolivet, J. A. Zimmerman, M. Y. Lee, F. D. Becchetti, E. F. Aguilera, E. Martínez-Quiroz, and J. D. Hinnefeld, *Phys. Rev. Lett.* **81**, 4580 (1998).
- [34] E. F. Aguilera, J. J. Kolata, F. M. Nunes, F. D. Becchetti, P. A. DeYoung, M. Gouppell, V. Guimarães, B. Hughey, M. Y. Lee, D. Lizcano, E. Martínez-Quiroz, A. Nowlin, T. W. O'Donnell, G. F. Peaslee, D. Peterson, P. Santi, and R. White-Stevens, *Phys. Rev. Lett.* **84**, 5058 (2000).
- [35] E. F. Aguilera, J. J. Kolata, F. D. Becchetti, P. A. DeYoung, J. D. Hinnefeld, Á. Horváth, L. O. Lamm, H.-Y. Lee, D. Lizcano, E. Martínez-Quiroz, P. Mohr, T. W. O'Donnell, D. A. Roberts, and G. Rogachev, *Phys. Rev. C* **63**, 061603(R) (2001).
- [36] V. Guimarães, E. N. Cardozo, J. Lubian, M. Assunção, K. C. C. Pires, L. F. Canto, B. Mukeru, G. Kaur, and E. F. Aguilera, *Eur. Phys. J. A* **57**, 90 (2021).
- [37] V. Guimarães, J. Lubian, J. J. Kolata, E. F. Aguilera, M. Assunção, and V. Morcelle, *Eur. Phys. J. A* **54**, 223 (2018).
- [38] E. F. Aguilera, I. Martel, A. M. Sánchez-Benítez, and L. Acosta, *Phys. Rev. C* **83**, 021601(R) (2011).
- [39] C. Y. Wong, *Phys. Rev. Lett.* **31**, 766 (1973).
- [40] B. T. Kim, M. Naito, and T. Udagawa, *Phys. Lett. B* **237**, 19 (1990).
- [41] W. Y. So, T. Udagawa, S. W. Hong, and B. T. Kim, *Phys. Rev. C* **77**, 024609 (2008).
- [42] A. Gómez Camacho, E. F. Aguilera, P. R. S. Gomes, and J. Lubian, *Phys. Rev. C* **84**, 034615 (2011).
- [43] A. Gómez-Camacho, E. F. Aguilera, J. Lubian, and P. R. S. Gomes, *J. Phys. G: Nucl. Part. Phys.* **40**, 035103 (2013).
- [44] A. Gómez Camacho and E. F. Aguilera, *Phys. Rev. C* **90**, 064607 (2014).
- [45] A. Gómez-Camacho and E. F. Aguilera, *Nucl. Phys. A* **735**, 425 (2004).
- [46] A. Gómez-Camacho, E. F. Aguilera, E. Martínez-Quiroz, P. R. S. Gomes, J. Lubian, and L. F. Canto, *Nucl. Phys. A* **833**, 156 (2010).